Dalton Transactions

ROYAL SOCIETY OF CHEMISTRY

PAPER

View Article Online
View Journal | View Issue

Cite this: *Dalton Trans.*, 2025, **54**, 16056

A coordinatively unsaturated mononuclear europium(III) complex: a luminescent sensor for adenosine monophosphate in aqueous media

Raju Biswas,[a] Manik Das, *[b,c] Toushique Ahmed, [c] Soumik Laha,[d] Bidhan Chandra Samanta,[e] Rosa M. Gomila, [f] Antonio Frontera, *[f] Goutam Pramanik*[g] and Tithi Maity *[b]

Luminescent probes for sensing adenosine monophosphate (AMP), particularly in the presence of ADP and ATP, are rare. Herein, we report a novel Eu(III) complex, $[(H_2O)(L)_2Eu(SO_3CF_3)_2](SO_3CF_3)$ (**EuC**), for this purpose, which is synthesized through the reaction of a urea and acyl hydrazone-based ligand **L** and Eu(III) triflate salt. Thorough characterization, including single-crystal X-ray diffraction analysis, reveals the coordinatively unsaturated structure of **EuC**. By taking advantage of this unsaturation, the said **EuC** complex can sense AMP in aqueous medium with a commendable LOD value of 0.412 μM, even in the presence of other anions, including several competitive phosphate anions. Only in the presence of AMP, the characteristic Eu(III)-centered emission peaks for the $^5D_0 \rightarrow {}^7F_J$ (J = 0–4) transitions, obtained upon irradiating the ligand center, are found to be significantly intensified, which further leads to the enhancement in the relative quantum yield and Eu(III)-centered lifetime values. Attempts are also made to shed light on the plausible mechanism of the AMP-sensing efficacy of **EuC**. The UV-vis absorption and fluorescence titration results suggest a probe–analyte adduct formation between **EuC** and AMP. The formation of such an adduct is further validated by ^{31}P and ^{19}F NMR spectroscopy, as well as DFT calculations (RI-BP86-D4/desf-TZVP level of theory). Interestingly, the existence of some non-covalent interactions between the ligand and the adenine base of AMP is found to be instrumental in the selective sensing mechanism by the said **EuC** complex, which is quite unprecedented in the literature.

Received 1st August 2025,
Accepted 19th September 2025

DOI: 10.1039/d5dt01849h

rsc.li/dalton

Introduction

Designing host molecules that selectively bind target anions in water and translating this binding into a measurable signal are the main hurdles in supramolecular anion receptor chemistry.[1–3] Research focuses on nucleoside phosphate anions, including ATP, ADP, AMP, GTP, GDP, and UDP, which are crucial for biological processes like DNA formation, energy transduction, cellular signalling, and phosphorylation.[4–7] Developing synthetic receptors that can differentiate these anions under physiological conditions is an innovative biomedical research and drug discovery approach.[8,9] However, similarities in the anion structure, size, and charge, combined with high hydration energies, pose significant challenges in this cutting-edge research field. Examples of receptors with high affinity and selectivity for particular nucleoside phosphate anions are uncommon but greatly sought due to their potential to advance the life sciences and medicine.[10] Synthetic receptors must compete with water molecules for negatively charged phosphate groups. As a result, synthetic receptors that demonstrate strong affinity and high selectivity for specific nucleoside phosphate anions are relatively scarce. If a metal–ligand complex is used for this detection, it can overcome the high hydration energies of phosphate anions in water.[11–13]

Many Zn(II) complexes have been explored for their ability to detect phosphates, particularly in aqueous media.[14–16] Research has shown that these complexes exhibit a detection response primarily towards adenosine triphosphate (ATP) and adenosine diphosphate (ADP). The sensing response of these

[a]*Indian Association for the Cultivation of Science, Jadavpur, Kolkata, West Bengal, India*
[b]*Department of Chemistry, Prabhat Kumar College, Contai, Purba Medinipur, West Bengal, 721404, India. E-mail: titlipkc2008@gmail.com*
[c]*Department of Chemistry, Jadavpur University, Jadavpur, Kolkata, West Bengal, India*
[d]*Indian Institute of Chemical Biology, Jadavpur, Kolkata, West Bengal, India*
[e]*Department of Chemistry, Mugberia Gangadhar Mahavidyaaya, Purba Medinipur, India*
[f]*Departament de Química, Universitat de les Illes Balears, Crta de Valldemossa km 7.5, 07122 Palma de Mallorca, Baleares, Spain. E-mail: toni.frontera@uib.es*
[g]*UGC DAE CSR, Kolkata, West Bengal, India. E-mail: goutam.pramanik@gmail.com*

Zn(II) complexes towards ATP and ADP is often attributed to some factors, including coordination interaction, H-bonding, and conformational changes. Meanwhile, the sensing of AMP by metal complexes is very rare. Significant advancements in anion selectivity have been made by incorporating a dual approach in receptor design, leveraging metal–ligand and hydrogen bonding interactions.[17,18] Lanthanide-based receptors offer a promising platform for designing selective anion receptors, where affinity and selectivity can be finely tuned through strategic modifications of the ligand structure, conformational flexibility, steric effects around the metal centre, and the overall charge of the complex.[19–22] Butler's research groups have developed Eu complexes[23,24] with supramolecular ligands with one or two anion binding sites for selective detection of ADP and ATP in an aqueous solution. Changes in the luminescence properties, including intensity, spectral shape, and lifetime, indicate anion binding efficacy. These variations arise from alterations in the coordination environment surrounding the lanthanide(III) ion.

The long-lived luminescence of Eu(III) and Tb(III) complexes, resulting from the Laporte-forbidden nature of f–f orbital transitions, enables their use in anion-sensing applications, even in complex biological environments like blood serum. Using time-gating techniques, the lanthanide-centered emission can be distinguished from the short-lived autofluorescence of biomolecules, allowing for enhanced signal-to-noise ratios and extremely low anion detection limits.

Acyl hydrazone and amide moieties have been individually employed as chemosensors for cation and anion detection.[25–30] However, combining these two components can potentially create a molecule capable of binding both cations and anions. Based on this concept, Albrecht *et al.*[31] developed a linear ligand featuring both amide and acyl hydrazone groups, which was then used to synthesize two dinuclear Eu- and Tb-based double-stranded helicates. Notably, the Eu complex, obtained *via* self-assembly of the ligand and Eu(III) salt, demonstrates the ability to detect AMP through turn-on fluorescence in a pure aqueous medium. This sensing phenomenon was attributed to the displacement of anions and water molecules by AMP, resulting in enhanced luminescence. Besides, the coordination between the nitrogenous adenine base and Eu(III) ion was also taken into consideration to comprehend the sensing mechanism. Despite this breakthrough, the development of a mononuclear Eu complex with a ligand incorporating acyl hydrazone and urea moieties for AMP detection in a pure aqueous medium remains unexplored.

Addressing the points, the present work demonstrates the development of a novel mononuclear europium(III) complex, **EuC**, through the coordination of urea and the acyl hydrazone-based ligand with europium(III) salts. Characterization using spectroscopic techniques and X-ray crystallography revealed **EuC**'s structure, featuring a nine-coordinate lanthanide complex with a specific arrangement of coordinating atoms. **EuC** exhibits a selective enhanced luminescence response to adenosine monophosphate (AMP), distinguishing it from other anions such as ADP, ATP, and others. The best possible sensing mechanism here involves the release of the corresponding counter anion and a water molecule from the coordination sphere and introduction of AMP, as supported by DFT calculations. Unlike the earlier reported case, the direct coordination between the Eu(III) ion and nitrogenous adenine base is not believed to be operative here, as indicated from both experimental and computational outcomes. Additionally, the plausible noncovalent interactions between the adenine base and the ligand are counted for the high selectivity of **EuC** towards AMP. In the cases of ADP and ATP, there is a possibility of steric hindrance, which may further create an obstacle for them to enter the coordination sphere of Eu. UV-vis and fluorescence spectroscopic titration confirm the formation of a probe–analyte adduct and elucidate the sensing mechanism. These findings demonstrate the potential of **EuC** as a selective luminescent sensor for AMP detection, with applications in biomedical research, diagnostic assays, and molecular recognition studies.

Results and discussion

Design and synthesis

Ligand **L** is developed by a three-step reaction where the reaction of 4-nitrophenyl isocyanate and 3-aminobenzoate produces intermediate **1**, and the reaction of **1** with hydrazine hydrate produces compound **2**. Finally, the reaction of compound **2** with pyridine-2-carboxaldehyde produces ligand **L**. The reaction of **L** and Eu(III) $(OTf)_3$ salt produces the target complex **EuC**. The total synthetic procedure is given in Scheme 1. The ^{1}H-NMR and mass spectral data of all the developed intermediates and ligand confirm their structural integrity in solution.

NMR spectroscopic analysis

The ^{1}H NMR and ^{13}C NMR spectra of compounds **1**, **2**, and **L** are given in Fig. S1–S7 in the SI. The NMR spectrum validates the formation of intermediates and ligand **L**. Although we have obtained the crystal of our target complex, we are interested in investigating the *in situ* complexation of $Eu(OTF)_3$ with our ligand **L**. For this purpose, we performed ^{1}H NMR titration of free **L** upon gradual addition of the Eu(III) salt. The experimental results are graphically presented in Fig. 1a and b. The titration results unveil that during the gradual addition of Eu(III) ions, the emine –CH proton (H_m) and the acylhydrazone –NH proton (H_k) are gradually shifted towards the upfield region, whereas the *ortho* and *meta* protons of the pyridine ring (H_l and H_n) are shifted towards the downfield region. Hence, it is obvious that our ligand **L** interacts with the Eu(III) ion, which further implies that in the solution state, the demetallation process is ruled out. It is noteworthy to mention here that the presence of a paramagnetic ion in a complex may sometimes lead to signal broadening in the NMR spectrum along with unpredictable multiplicity alteration, although it is not applicable in every case with a paramagnetic ion. In the

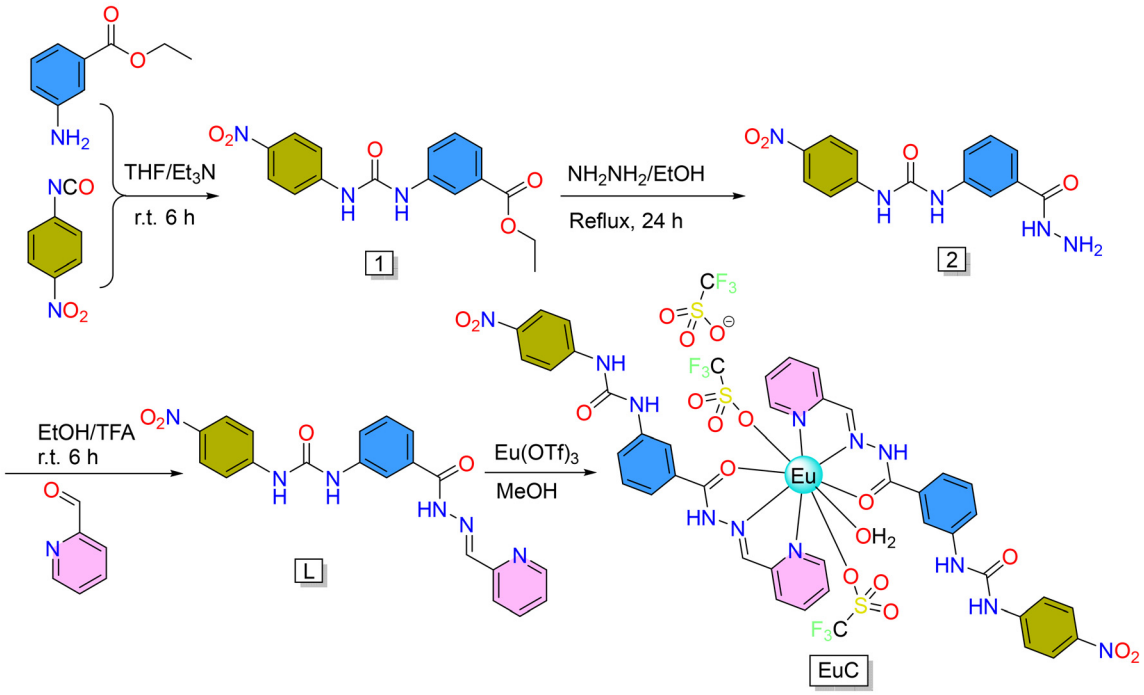

Scheme 1 Synthesis of L and **EuC**.

present case, the signal for the H_l proton is noticed to undergo signal broadening along with multiplicity alteration (Fig. 1a), unlike the rest of the signals. These observations are in line with earlier reported literature comprising such luminescent Eu(III) complexes.[33,34] The NMR spectral change at the point of 0.5 equivalent Eu(III) addition to the ligand **L** is well matched with the ^{1}H NMR spectrum of the isolated complex (Fig. S8), which strongly supports the formation of the said complex.

Mass spectra

The ESI mass spectral data of compounds **1**, **2**, and **L** are collected in DMSO solvent. The mass spectra of all three complexes are in the SI in Fig. S9–S11. All three compounds **1**, **2**, and **L** show three peaks at *m*/*z* 530.1086, 516.1054, and 405.1317, which correspond to the structures of the species $[C_{16}H_{16}N_3O_5]^+$, $[C_{14}H_{14}N_5O_4]^+$, and $[C_{20}H_{17}N_6O_4]^+$, respectively.

The mass spectrum is recorded in DMSO solvent for structural confirmation of the **EuC** complex in the solution and is presented in Fig. 2. A peak at *m*/*z* = 854.9464 is observed, which may be attributed to the fragment (**EuC** – OTF^- – H_2O – **L**)$^+$. The corresponding experimentally observed and theoretically simulated isotopic distribution patterns of the said peak are also found to resemble well with each other.

Single crystal structure analysis of EuC $[Eu(L)_2(OTf)_2(H_2O)](OTf)$

Single-crystal X-ray diffraction was performed with a Bruker D8 Venture diffractometer, equipped with a MoKα radiation source and a PHOTON III detector. The structure is solved using ShelXT and refined with ShelxL programs using Olex2 as a graphical user interface.

A single crystal suitable for diffraction is grown from the methanolic solution of the **EuC** complex by the diffusion of diethyl ether. The prism-shaped crystal appeared after 7 days at ambient temperature. The complex crystallizes in the triclinic cell system, $P\bar{1}$ space group, with crystallographic parameters, a = 13.1729(13) Å, b = 15.8006(17) Å, c = 17.7785(19) Å, α = 110.990°(3), β = 108.537°(3), γ = 91.304°(3), and V = 3236(6) Å^3. The details of crystallographic parameters are summarized in Table 1.

The asymmetric unit of the **EuC** complex is associated with two ligands (N,N,O donor), one Eu(III) metal, two counter triflate anions coordinated to the metal center, one counter triflate anion hydrogen bonded with the urea group of the ligand, one water molecule coordinated to the metal center and two diethyl ether molecules present in the crystal structure but does not interact directly with the metal center and does not play any important role in the crystal structure (Fig. 3a). The Eu–metal center is coordinatively unsaturated as europium(III) has the highest coordination up to twelve and in the present case the Eu is nine coordinated. The geometry surrounding europium(III) ions is characterized as a spherical capped square antiprism, resembling a muffin-like structure, as determined using continuous shape measures (CShMs) analyzed using Shape 2.1 software[32] (Table S1) (Fig. 3b and c). The SCXRD analysis showed that the E–O bond distances around the Eu-centre vary from 2.394(4) to 2.420(3) Å, while the Eu–N bond distances around the Eu-centre vary from 2.577(4) to 2.610(4) Å as can be seen in Fig. 3 and Table S2.

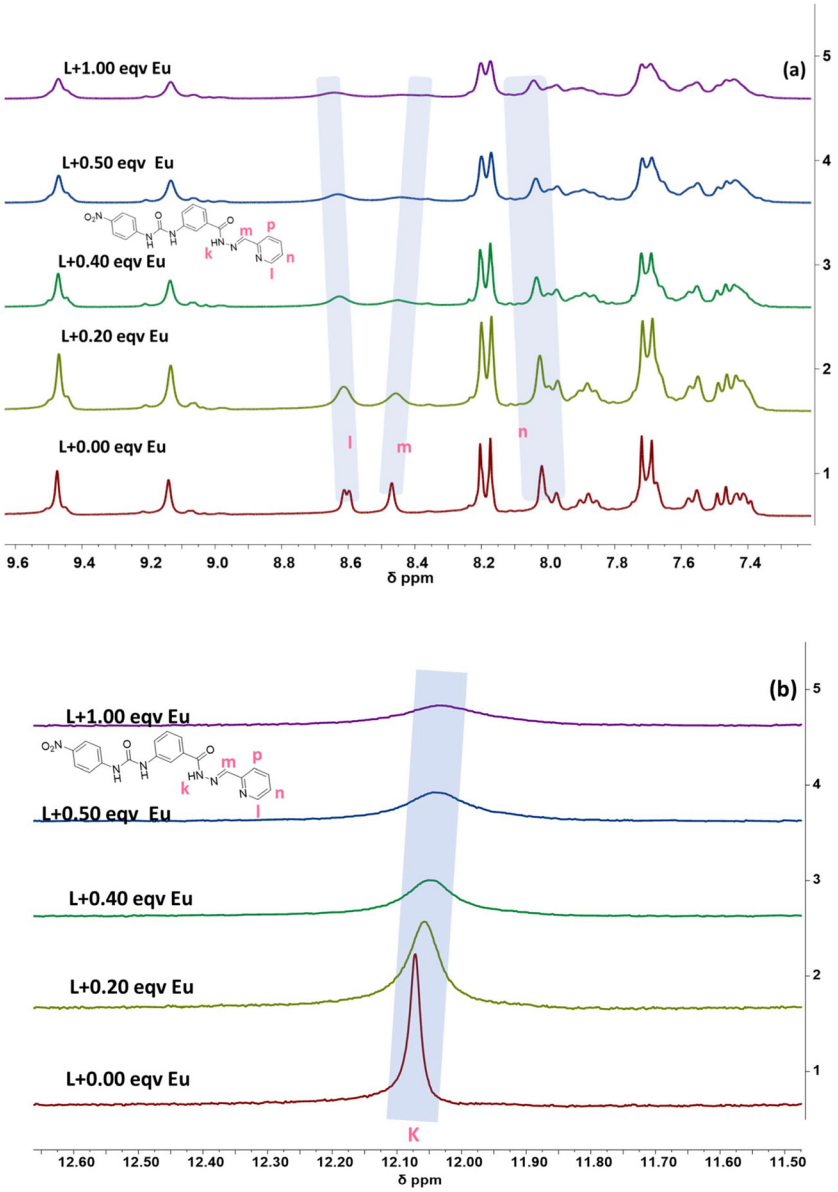

Fig. 1 ^{1}H NMR spectrum of L (2 μM) upon the gradual addition of Eu(III) ions (0–1 equiv.) in DMSO-d_6 (500 MHz, 298 K).

After careful observation of the **EuC** complex, we tried to investigate the packing of the crystal. Interestingly, we found that the **EuC** units are linked together with several classical and nonclassical hydrogen bonding interactions where two oxygen atoms of the coordinated CF_3–SO_3 groups from one unit participated in the intermolecular H-bonding interaction (2.096–2.164 Å) with the NH atoms of the urea part of the second unit. On the other hand, the oxygen atom of the NO_2 groups are also involved in the intermolecular H-bonding interaction (2.007 Å) with the NH atoms of the acyl hydrazone part of the complex (Fig. 4a). Adjointly, these interactions showcase the formation of the 2D network of the complex (Fig. 4b and c). The two urea units of the two ligands are *trans* to each other, which favors the formation of a 2D network. In the complex, there are two ligand units; among them, one urea part is involved in the intermolecular H-bonding, while the remaining part is involved in the intramolecular H-bonding with the non-bonded counter CF_3–SO_3 group.

Meanwhile, this interaction also facilitates the positioning of the counter anion, ensuring the overall neutrality of the complex. Additionally, it provides extra stability to the complex through hydrogen bonding. The relevant hydrogen bonding parameters are summarized in Table S3, SI.

Photophysical properties of the ligand and EuC

After the successful characterization of the ligand and the complex **EuC**, we explored their photophysical properties. To this end, we recorded their absorption and steady-state

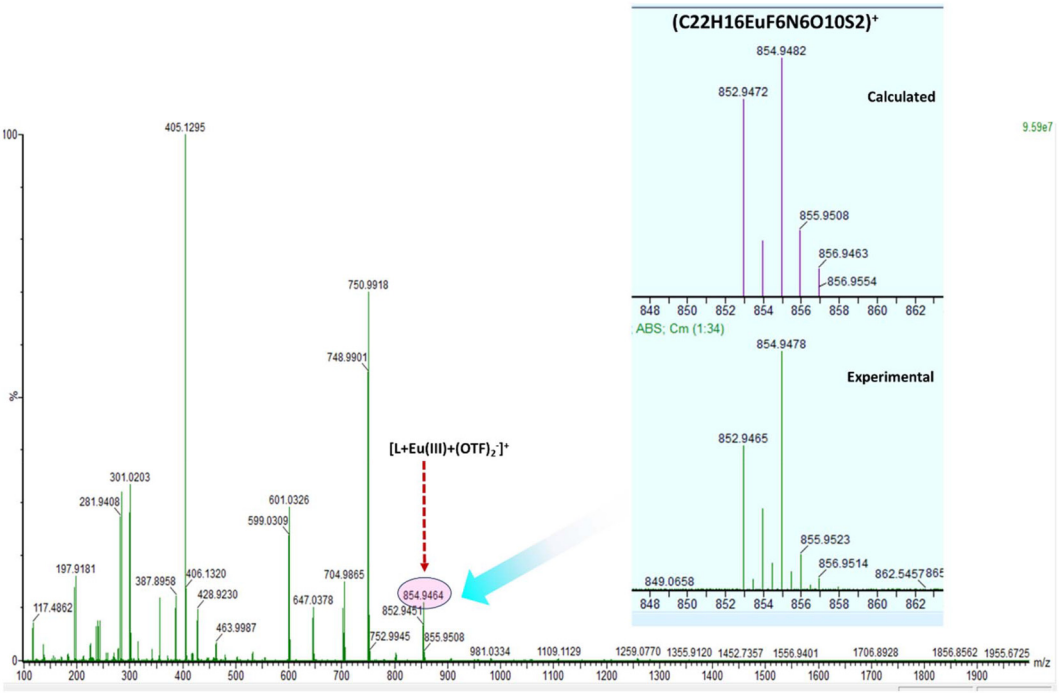

Fig. 2 HRMS data of **EuC** in DMSO. The upper right portion indicates the simulated (calculated) and the lower right portion depicts the observed isotopic distribution patterns.

Table 1 Crystal data and structure refinement for mo_PG120724_0m_a (**1**)

Identification code	mo_PG120724_0m_a (**1**) CCDC 2414539
Empirical formula	$C_{51}H_{44}EuF_9N_{12}O_{20}S_3$
Formula weight	1564.12
Temperature/K	172.59
Crystal system	Triclinic
Space group	$P\bar{1}$
a/Å	13.1729(13)
b/Å	15.8006(17)
c/Å	17.7785(19)
α/°	110.990(3)
β/°	108.537(3)
γ/°	91.304(3)
Volume/Å^3	3236.4(6)
Z	2
ρ_{calc}/g cm^{-3}	1.605
μ/mm^{-1}	1.172
F(000)	1572.0
Crystal size/mm^3	0.13 × 0.12 × 0.11
Radiation	MoKα (λ = 0.71073)
2Θ range for data collection/°	4.506 to 53.754
Index ranges	$-13 \le h \le 16$, $-20 \le k \le 20$, $-22 \le l \le 22$
Reflections collected	38 680
Independent reflections	13 847 [R_{int} = 0.0693, R_{sigma} = 0.0829]
Data/restraints/parameters	13 847/73/878
Goodness-of-fit on F^2	1.077
Final R indexes [$I \ge 2\sigma(I)$]	R_1 = 0.0532, wR_2 = 0.1222
Final R indexes [all data]	R_1 = 0.0856, wR_2 = 0.1480
Largest diff. peak/hole/e Å^{-3}	2.02/−1.49
CCDC number	2414539

emission spectra in aqueous solution at room temperature which are depicted in Fig. 5 and S12, respectively. The absorption spectrum of the free ligand reveals two absorption peaks at ~300 nm and 348 nm (Fig. S12). The band at ~300 nm may be attributed to π–π* transition, whereas the band at ~348 nm is ascribed to n–π* transition within the ligand framework. Upon complexation, the two absorption maxima are found to undergo a slight red shift of ~10 nm together with a broadening (Fig. 5a). Upon exciting the complex at 360 nm, characteristic peaks associated with f–f intraconfigurational transitions are observed, albeit with not so high intensities (Fig. 5b). To be specific, the peaks at 579 nm, 590 nm, 614 nm, 648 nm, and 697 nm are due to the $^5D_0 \rightarrow {}^7F_{J\ (J=0-4)}$ transitions of Eu(III) ions, respectively. This observation indicates the 'antenna effect' of the ligand. Since the f–f transitions of the lanthanide(III) ions are both spin and parity forbidden in nature, their direct excitation leads to very poor absorption (ε < 10 M^{-1} cm^{-1}) which in turn results in a very weak emission. To circumvent this problem, a high-energy absorbing organic chromophore (ε > 10 000 M^{-1} cm^{-1}) is brought into play, which efficiently absorbs light and transfers that to its coordinated lanthanide (III) ion. This indirect sensitization phenomenon is referred to as the 'antenna effect'.[33–35]

To confirm the development of the Eu(III) complex, we further measured the lifetime and relative quantum yield of the free ligand and the resulting complex. The lifetime of the free ligand is found to be 2.19 ns, whereas the lifetime of the

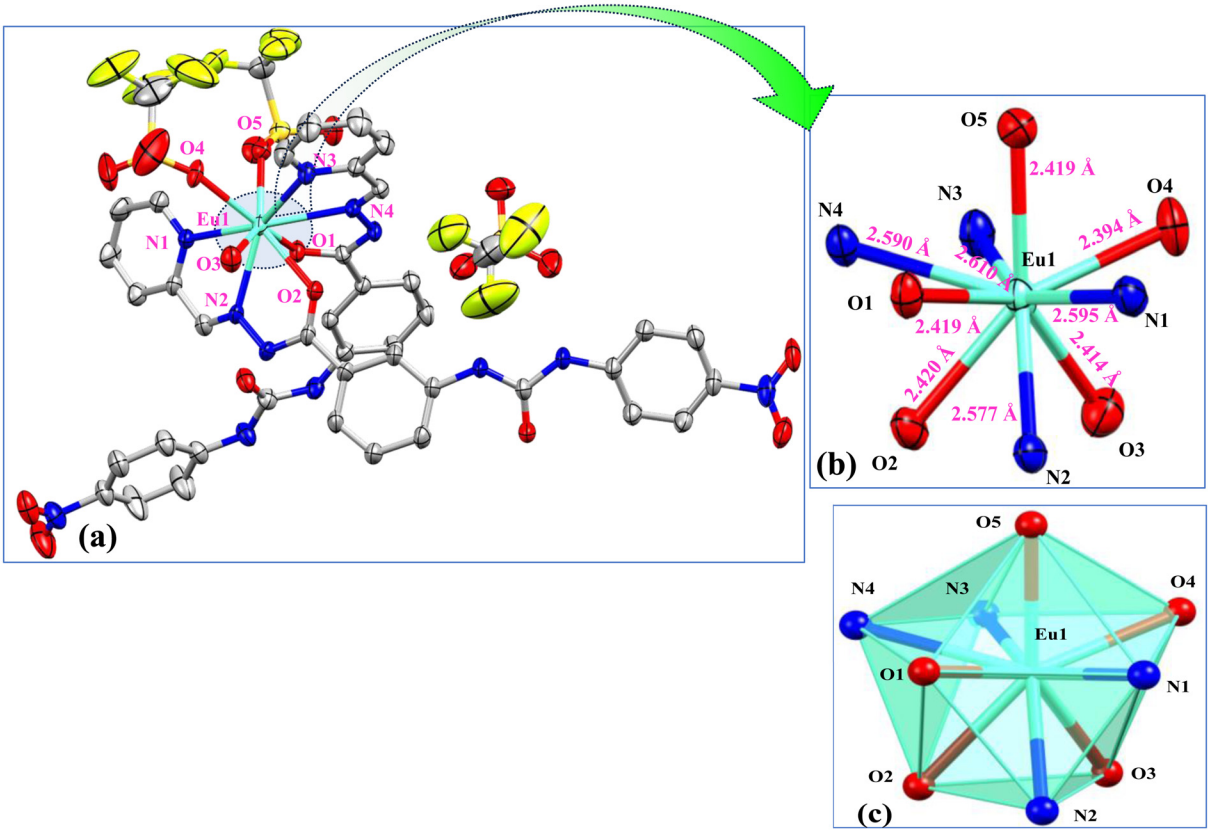

Fig. 3 (a) The Oak Ridge thermal-ellipsoid plot (ORTEP) view of the asymmetric unit of the **EuC** complex with 50% ellipsoid (all H atoms and the diethyl ether molecules are hidden for the better clarity of the crystal). (b) Connectivity of coordinating atoms (N and O) towards the Eu(III) center displaying the distorted tricapped trigonal prism (TCTP) geometry. (c) An overall polyhedron view of the complex towards the metal center.

Eu(III) complex is found to be 250 μs (Fig. S13). Besides, the relative quantum yield is also found to increase from 0.023 (for free ligand) to 0.101 (for **EuC**). The influence of pH on the photoluminescence behavior of the **EuC** complex is also explored. Among the Ln(III)-centered f–f intraconfigurational transitions, the electric dipole (ED) transition is different from the rest. The intensity of the peak corresponding to this ED transition is very sensitive to the symmetry of the central lanthanide(III) ion. The lower the symmetry, the higher the intensity of this very peak. Hence, we monitored the alteration of the intensity of the peak (at 614 nm) related to the ED transition ($^5D_0 \rightarrow {}^7F_2$) for Eu(III) in water upon varying the pH from 2 to 13 (Fig. S14). The results revealed that the maximum intensity is achieved in the pH range 7–9, coinciding with the physiological pH domain. This finding encourages us to consider the **EuC** complex as a sensor for the physiological conditions.

Response of EuC during sensing of AMP

To explore the potential sensing efficacy of the complex **EuC**, we considered recording its steady-state emission spectra upon adding up to 10 equiv. of various anions *viz.*, F^-, Cl^-, Br^-, I^-, SO_4^{2-}, NO_3^-, SCN^-, N_3^-, PO_4^{3-}, CO_3^{2-}, HPO_4^{2-}, AMP, ADP, ATP, glucose, NaDPH, and GMP separately. The corresponding emission spectral profiles, as depicted in Fig. 6, shows a remarkable emission enhancement of the complex only in the presence of AMP. On the other hand, no considerable luminescence alteration is observed in the presence of the other anions, even in the cases of ADP and ATP. The addition of AMP also resulted in an enhancement of the relative quantum yield (Φ) value from 0.101 to 0.234. This selective sensing of **EuC** is further validated by the competitive experiments (Fig. S15) where it has been observed that the emission intensity of the probe–AMP assembly remained practically unaffected in the presence of other competitive anions in an aqueous HEPES buffer medium at pH 7.4.

Before further monitoring of the sensing phenomena of **EuC** towards the AMP, the hydrostability of **EuC** should be checked. For this purpose, we recorded the emission intensity change of **EuC** in HEPES buffer (at pH 7.4) as a function of time. The experimental results are summarized in Fig. S16. The figure shows a minimal change in the emission intensity of **EuC** as a function of time, suggesting its excellent hydrostability. Here we further monitored the pH effect during AMP detection, and again recorded the emission intensity change

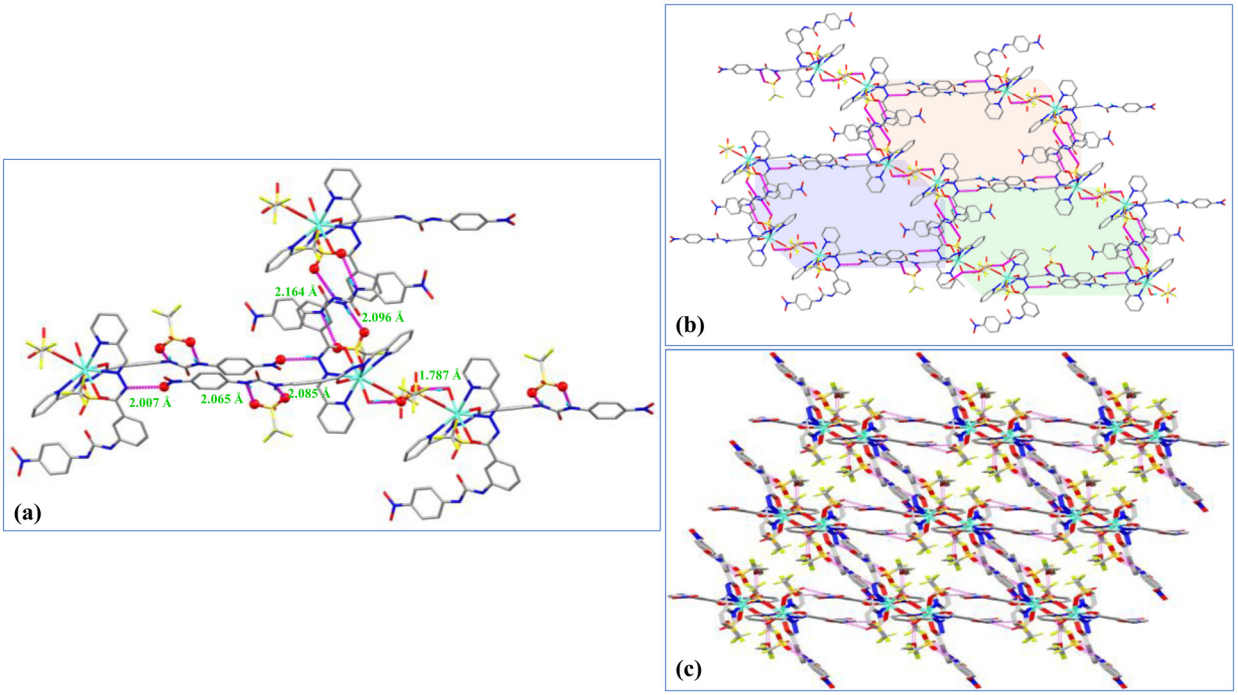

Fig. 4 (a) An overall view of the packing diagram of **EuC** along the *b*-axis showing the 2D network *via* intermolecular H-bonding interaction. (b and c) Visualization of both the intra- and intermolecular hydrogen bonding interactions (pink colour) (donor atoms are shown in a ball style and all the H-atoms are hidden for better clarity of the interactions except those H-atoms participating in H-bonding).

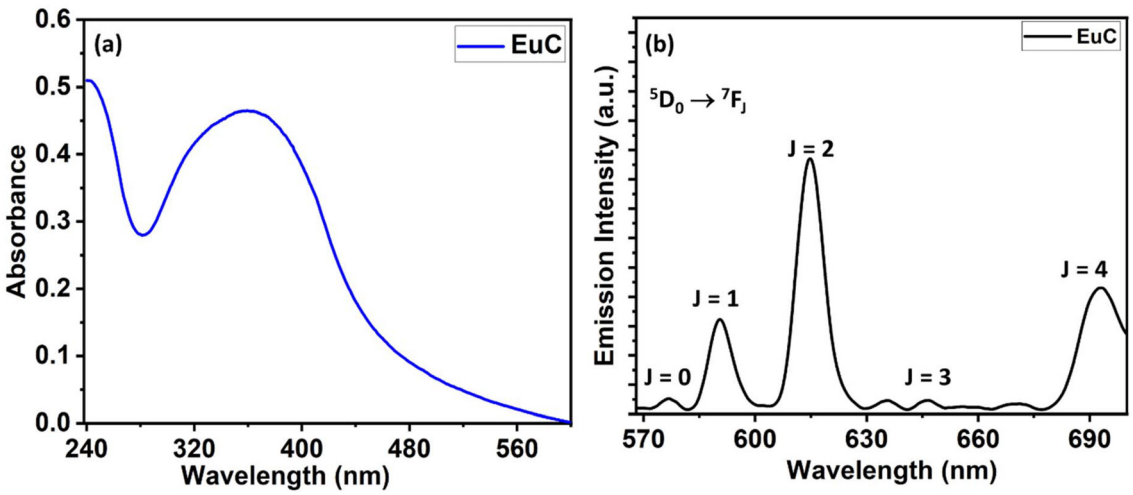

Fig. 5 The recorded (a) UV spectrum of **EuC** (5 μM) and (b) fluorescence spectrum of **EuC** (5 μM) in pure aqueous medium.

of **EuC** in the presence of AMP at different pH values. The results (Fig. S14) disclose the fact that the effective AMP detection ability is seen at pH 5.5–8.0. After that, we monitored the remaining sensing process, maintaining the pH at 7.4. The potential binding between the **EuC** complex and AMP is further investigated upon incremental addition of AMP (0.5 equiv. to 5 equiv.) onto a 5 μM aqueous solution of **EuC** in HEPES buffer medium. The interaction is monitored *via* the changes in the spectral profile during absorption and emission spectroscopic titrations displayed in Fig. 7 and 8. Free **EuC** shows a broad absorption band at ~360 nm. After the gradual addition of AMP to the solution of **EuC**, the lowest energy absorption band at 360 nm systematically decreases along with a slight red shift, whereas a new band appears at ~260 nm. This red-shifting indicates stabilization of the excited state of the complex upon the addition of AMP. The binding constant value is determined to be 3.62×10^4 M^{-1}, obtained by using the Benesi–Hildebrand (B–H) equation (eqn (1)).

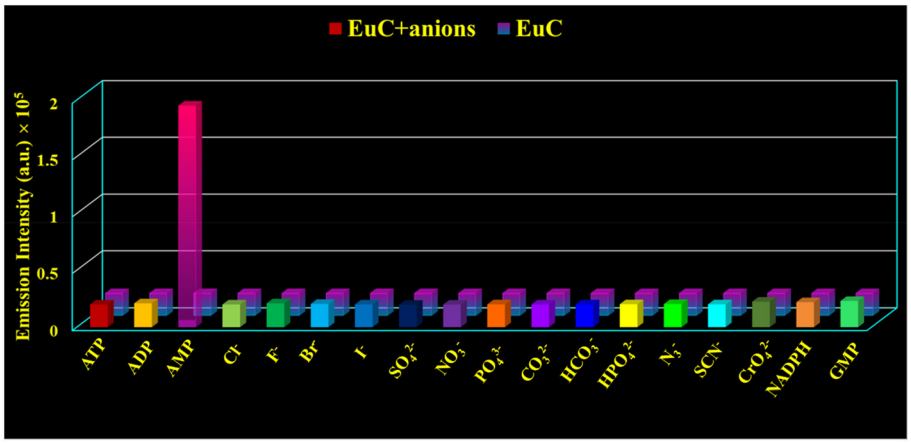

Fig. 6 The signature of the emission intensity of **EuC** (5 μM) at 614 nm upon the addition of 25 μM various anions in HEPES buffer (at pH 7.4) upon excitation at λ_{ex} = 360 nm.

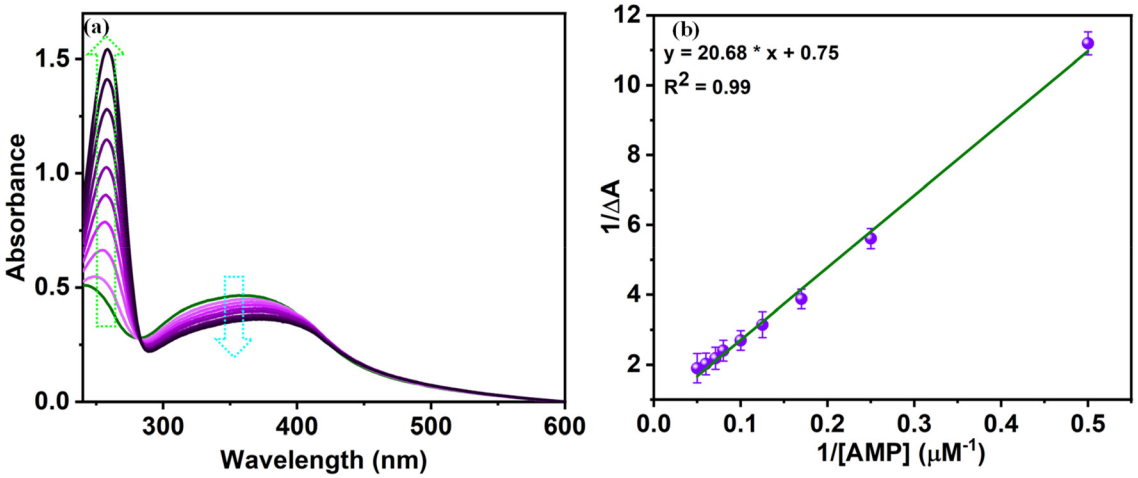

Fig. 7 (a) Change in the absorbance of **EuC** (5 μM) after gradual addition (1 μM–20 μM) of AMP in HEPES buffer medium at pH 7.4. (b) B–H curve to determine the probe–analyte binding constant.

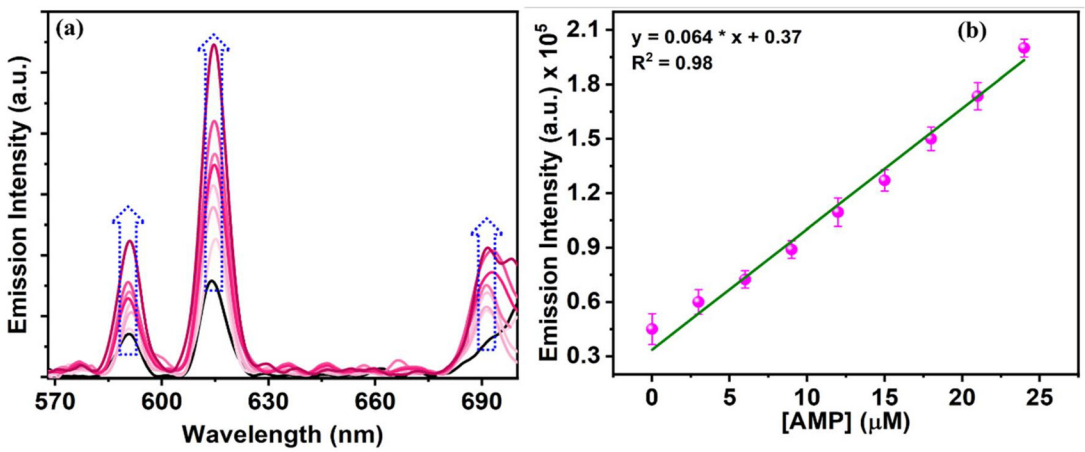

Fig. 8 (a) Evolution of the Eu(III)-centered emission in **EuC** (5 μM) at 580 nm, 614 nm, and 697 nm after step-wise addition of AMP (2 μM–25 μM) in HEPES buffer at pH 7.4 at λ_{ex} = 360 nm, showing the emission enhancement. (b) Emission intensity *vs.* [AMP] plot to determine the LOD value in AMP detection.

$$\frac{1}{A-A_0}=\frac{1}{(A_0-A_{max})K_b\times C}+\frac{1}{(A_0-A_{max})} \quad (1)$$

The absorbance values of probe **EuC** in different situations are denoted as follows:

A_0: absorbance in the absence of AMP; A: absorbance in the presence of AMP; A_{max}: absorbance at the saturation point of **EuC**–AMP interaction and C: the concentration of incorporated AMP.

In the case of the steady-state emission spectroscopic titration, upon exciting at ~360 nm, systematic intensification of the Eu(III)-centered peaks is noticed (Fig. 8a) upon the gradual addition of AMP into the 5 μM aqueous solution of **EuC** in HEPES buffer medium. The peak at 614 nm for the electric dipole transition is found to be most augmented, indicating the reduction of symmetry around the Eu(III) ion upon the addition of AMP. The probe–analyte binding constant K_b is measured by utilizing the titration profile according to the following B–H equation (eqn (2)).

$$\frac{1}{F-F_0}=\frac{1}{(F_0-F_{max})K_b\times C}+\frac{1}{(F_0-F_{max})} \quad (2)$$

F_0: fluorescence intensity of **EuC** in the absence of AMP; A: fluorescence intensity of **EuC** in the presence of AMP; A_{max}: fluorescence intensity at the saturation point of **EuC**–AMP interaction; and C: the concentration of incorporated AMP.

The measure binding constant is 3.38×10^4 M^{-1} (Fig. S17). The titration profile is further used to determine the limit of detection (LOD) during AMP recognition. The LOD can be determined by using eqn (3).[36] The measured LOD is 0.412 μM.

$$LOD=3\sigma/K \quad (3)$$

where σ is the standard deviation of the intercept obtained from the emission spectra of the blank **EuC** solution and K is the slope between the fluorescence intensity *versus* the analyte's concentration (Fig. 8b).

The sensing efficacy of **EuC** is further validated through fluorescence lifetime measurements. The results showed that **EuC** exhibited a mono-exponential decay with a lifetime of 250 μs. Upon the addition of AMP, the enhancement of lifetime is visualized from 250 μs to 360 μs, indicating the formation of a new species during the sensing process (Fig. S13).

Hence, the spectroscopic titration profiles, as well as the probe–analyte binding constant values, indicate a plausible interaction between **EuC** and AMP.

Plausible mechanism for EuC–AMP binding

We are now interested in understanding the binding mechanism between **EuC** and AMP. Despite our several attempts, we are unable to grow suitable single crystals that can confirm the structure and the binding nature of the probe–analyte assembly. However, the Job's plot analysis confirmed the formation of a 1 : 1 probe analyte adduct (Fig. S18). By examining the emission spectral changes upon the addition of AMP, we infer that AMP replaces any quencher co-ligand of Eu(III). Herein, one water molecule is present, which has often been found in the literature to act as a quencher if it is present in the vicinity of the lanthanide(III) ion.[37] So, one can consider this replacement of the water molecule to be responsible for the emission enhancement. The crystal structure of free **EuC** displays two ligands with a tridentate nature (N, N, O), two triflate ($CF_3SO_3^-$) anionic co-ligands, and a water molecule in the first coordination sphere of Eu(III). The AMP molecule usually coordinates in a bidentate fashion *via* the two O-atoms of its PO_4^{3-} moiety. Hence, two monodentate co-ligands should be released to welcome this AMP molecule into this coordination sphere of Eu(III). In line with this, it seems that a triflate anionic co-ligand also leaves the coordination sphere along with the water molecule. Another noticeable fact is that the extent of intensification of the peak related to the electric dipole transition is much higher than the rest of the Eu(III)-centered emission peaks. This may be attributed to the fact that the incorporation of AMP, along with the elimination of a water molecule and a triflate anion, could also result in reduction of the local symmetry around the Eu(III) ion. We further investigated the AMP recognition potential of **EuC** through ^{31}P NMR and ^{19}F NMR studies. The ^{31}P NMR results (Fig. S19) reveal that the free AMP shows a peak at −0.4465 ppm, while after binding with **EuC**, the NMR peak shifted about 0.1298 ppm towards the downfield region. Earlier literature reports[38] already disclosed that when AMP binds to the metal complex, the ^{31}P NMR peak shifts towards the downfield region, which supports our results. The ^{19}F NMR results (Fig. S20) reveal that the **EuC** shows a peak at −77.7319 ppm when two OTF anions are coordinated, while after binding with AMP, the NMR peak of the **EuC**–AMP adduct shifted towards the upfield region to some extent, which suggests that in this process OTF anions become decoordinated. From the literature, we find that the free OTF anion shows an ^{19}F NMR peak at ~78–79 ppm. In our present study, we found that the NMR signal shifted towards the upfield region, which may be due to some decoordination of the OTF anion. The DFT analysis also substantiates this mechanistic possibility, as will be discussed in the following section. The structure of the **EuC**–AMP adduct has been optimized through density functional theory (DFT) studies, and is schematically represented in Scheme 2. Notably, unlike AMP, ADP and ATP could not take part in the binding course. We believe that the steric hindrance factor for the latter two molecules is responsible for this incapability. It is also noteworthy to mention that the urea moiety cannot bind to AMP due to the already present H-bonding between urea NH and a triflate anionic co-ligand in the free **EuC**. Furthermore, the specificity of **EuC** towards AMP is explained by another point of view, which is explained in the following section.

The spectroscopic results and Job's plot analysis results strongly suggest the formation of a 1 : 1 probe–analyte adduct. Our observations, particularly the marked enhancement of the electric dipole transition peak, point to a reduction in local symmetry around the Eu(III) ion upon binding with AMP. While the primary coordination appears to be through the

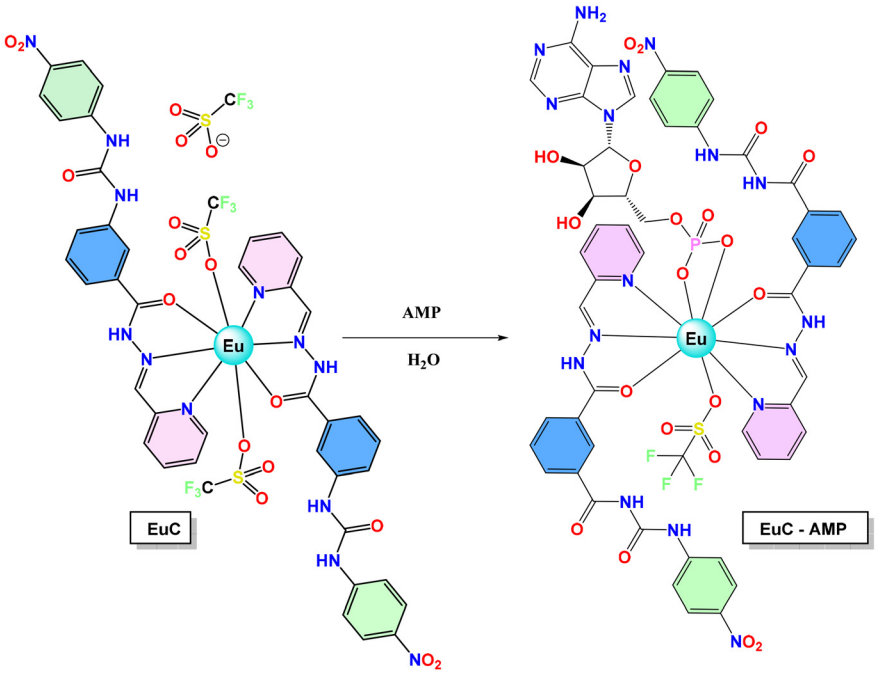

Scheme 2 Schematic representation of plausible coordination of AMP to **EuC**.

phosphate moiety of AMP, the high selectivity observed for AMP over ADP and ATP, despite their similar phosphate groups, suggests that other factors are at play. We hypothesize that noncovalent interactions between the adenine base of AMP and the ligand of the **EuC** complex are crucial for this selectivity. These interactions likely contribute to the overall stability of the **EuC**–AMP adduct, creating a more favorable binding environment that is not as accessible to the bulkier ADP and ATP molecules due to steric hindrance.

Thus, while the sensing mechanism for the earlier reported dinuclear Eu(III)-based double-stranded helicate system comprises the direct coordination of the adenine base with the Eu (III) ion, the present mononuclear Eu(III)-based probe offers an additional factor toward the AMP-selectivity *via* the noncovalent interactions between the adenine base and the ligand.

DFT study

DFT calculations were performed to analyze the binding modes of AMP to the **EuC** complex, considering two possibilities. The first involves the replacement of one weakly coordinated triflate anion and the water molecule by the phosphate group of AMP in a bidentate fashion, as depicted in Scheme 2. The second possibility explores the replacement of both triflate anions by AMP. For these optimizations, we employed the RI-PB86-D4/def2-TZVP level of theory, which offers a good balance between computational efficiency and accuracy for systems of this size. The chosen basis set accounts for scalar relativistic effects through effective core potentials (ECPs) (see the Computational details section).

Fig. 9a illustrates the adduct in which AMP (binding mode 1) replaces one triflate and one water molecule, resulting in an electroneutral adduct. The reaction energy computed in solvent for the replacement of CF_3–SO_3^- and H_2O by AMP–is -30.8 kcal mol^{-1}, indicating that this substitution is energetically favorable. In this configuration, both the adenine and ribose moieties of AMP interact with the hydrazone-based ligands. Specifically, the NH_2 group of adenine forms two hydrogen bonds with the nitrophenyl group (NH···O and CH···N), with distances characteristic of typical H-bonds. Additionally, the oxygen atom of ribose establishes an LP···π interaction with the Eu-coordinated pyridine ring, a type of contact commonly found in DNA and associated with stabilizing the Z-form. These noncovalent interactions, combined with the strong Eu···O coordination bonds formed by the phosphate group, significantly contribute to the stability of this adduct. This highlights an advantage of AMP over inorganic anions, which can only form coordination bonds by replacing the triflate and (or) water molecules. Although similar interactions are possible for ADP or ATP, the additional phosphate units in these molecules likely reduce their ability to establish comparable contacts due to the increased flexibility and length of their phosphate arms. Furthermore, analysis of the optimized adduct in Fig. 9a reveals that interligand NH···O hydrogen bonds between the urea and hydrazone groups contribute to stabilizing the structure, even though these interactions do not directly involve AMP.

The second binding mode analyzed (Fig. 9b) involves AMP replacing both triflate counterions in a bidentate fashion. However, this configuration is significantly less energetically favorable (-21.8 kcal mol^{-1}). The adenine ring establishes

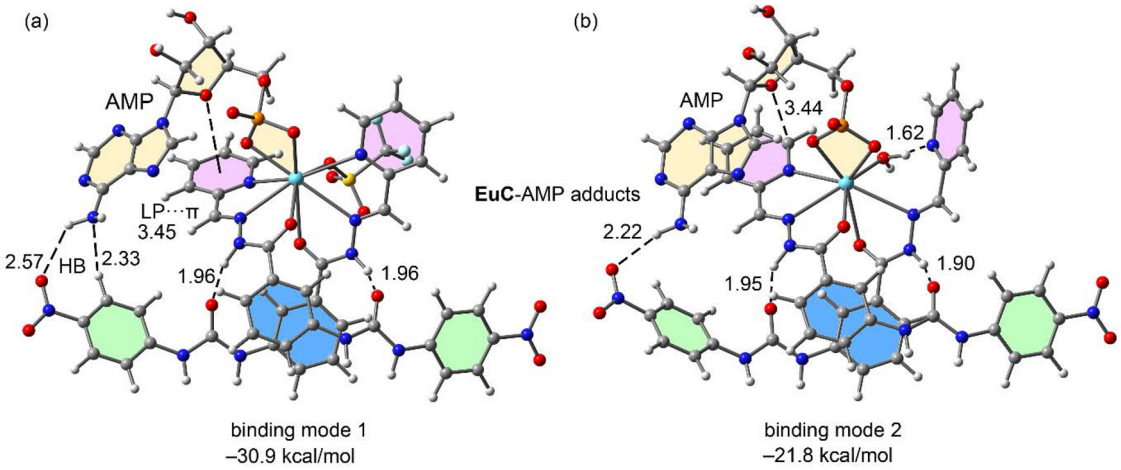

Fig. 9 RI-PB86-D4/def2-TZVP optimized geometries of two **EuC**–AMP assemblies, without (a) and with a coordinated water molecule (b). Distances are in Å.

fewer noncovalent interactions with the **EuC** complex in this mode, forming only an NH···O contact without the accompanying CH···N interaction. Moreover, the LP···π interaction between ribose and the pyridine ring is absent, with the oxygen atom of ribose instead forming a weaker interaction with a single carbon atom of the pyridine. Additionally, one Eu···N coordination bond is disrupted due to the proximity of the coordinated water molecule and AMP's binding, causing the N atom of pyridine to form a short OH···N hydrogen bond with the water molecule instead of coordinating to Eu(III).

Conclusion

In summary, we have synthesized and successfully characterized a novel mononuclear Eu(III) complex, **EuC**, featuring a urea-functionalized ligand, for selective AMP sensing in an aqueous environment. The structural and spectroscopic studies revealed that the unsaturated coordination environment around the Eu(III) center enables selective recognition of AMP through the enhancement of emission intensity and lifetime of the said complex. This selectivity arises from a combination of steric and electronic effects, which prevent ADP and ATP from effectively interacting with the Eu(III) center. The selective binding of AMP to **EuC**, confirmed through UV-vis and fluorescence spectroscopic titration, competitive assays, and DFT calculations, highlights the critical role of noncovalent interactions, such as hydrogen bonding and LP···π interactions, in stabilizing the **EuC**–AMP adduct. This stabilization of the **EuC**–AMP adduct is also reflected in the absorption spectroscopic titration.

Hence, the photophysical investigation on **EuC** demonstrated swift sensitivity and an ultralow-level detection limit for AMP, making it a promising candidate for biological and analytical applications, including diagnostic assays and molecular recognition studies. Future studies will focus on exploring the applicability of **EuC** in complex biological environments and expanding its sensing capabilities to other nucleotide phosphates.

Experimental section

Materials and methods

All reagents were purchased from commercial sources (Sigma-Aldrich and TCI) and the solvents were dried under standard procedures. All inorganic salts were obtained as molecular biology-grade chemicals from Sigma Aldrich.

Physical measurements

^{1}H NMR spectra were recorded in Bruker 400 and 500 MHz and Bruker Avance 600 operating at 400 MHz and 500 MHz, respectively. ^{13}C NMR spectra were recorded in Bruker 400 and 500 operating at 101 MHz and 126 MHz. Chemical shifts are reported in parts per million (ppm) relative to their residual solvent peaks (DMSO-d_6: δ_H = 2.50 ppm, δ_C = 39.9 ppm). High-resolution ESI mass spectrometry (HRMS) analyses were performed in a Waters Q-TOF instrument. Single crystal X-ray diffraction data were collected at 173 K on a Bruker diffractometer equipped with MoKα-radiation. In the present work, the elemental (C, H, and N) analysis was performed by using a PerkinElmer 2400II elemental analyzer. Bruker Tensor 27 was utilized to gather FTIR data in ATR mode. A Shimadzu 1900i spectrophotometer was utilized for the electronic absorption investigation. The Perkin Elmer fluorescence spectrometer FL6500 was utilized for all of the fluorescence spectroscopic investigations in quartz cuvettes having a path length of 1 cm. Luminescence lifetime measurements were carried out by using a 370 nm spectral LED source *via* the multi-channel scaling (MCS) technique from the Horiba Deltaflex setup with a TBX picosecond photon detection module, and the luminescence decay data were analyzed by using Eztime software.

Synthesis of intermediate 1

4-Nitrophenyl isocyanate (496 mg, 3 mmol) was taken in a 100 ml RB flask and dissolved in 20 ml dry THF. Then ethyl-3-aminobenzoate (500 μl, 3 mmol) was added to the mixture and the reaction mixture was stirred at r.t. for another 6 h. A white precipitate appeared slowly. It was filtered with filter paper and the residue was washed with diethyl ether. A white solid was obtained as a pure product (1250 mg, yield: 87%). ^{1}H NMR: (500 MHz, DMSO) δ 9.46 (s, 1H), 9.18 (s, 1H), 8.24–8.15 (m, 3H), 7.73–7.66 (m, 3H), 7.62 (dt, J = 7.8, 1.4 Hz, 1H), 7.46 (t, J = 7.9 Hz, 1H), 4.32 (q, J = 7.1 Hz, 2H), 1.33 (t, J = 7.1 Hz, 3H). ^{13}C: NMR: (126 MHz, DMSO) δ 166.08, 152.45, 146.64, 141.62, 139.92, 130.99, 129.71, 125.56, 123.58, 119.46, 118.12, 61.27, 14.63. HRMS: calcd for $C_{16}H_{16}N_3O_5$ 330.1090, found 330.1086.

Synthesis of intermediate 2

Intermediate **1**, ethyl 3-(3-(4-nitrophenyl)ureido)benzoate (300 mg, 0.911 mmol), was taken in a 100 ml RB flask and 20 ml dry EtOH was added to it to make a suspension. Then excess hydrazine hydrate was added to the mixture and the reaction mixture was refluxed for another 24 h. A white precipitate appeared slowly. It was filtered with filter paper and the residue was washed with diethyl ether. A white solid was obtained as a pure product (260 mg, yield: 90%). ^{1}H NMR: (400 MHz, DMSO) δ 9.75 (s, 1H), 9.10 (s, 1H), 8.20 (d, J = 9.0 Hz, 2H), 7.90 (s, 1H), 7.71 (d, J = 9.0 Hz, 2H), 7.63 (dd, J = 7.9, 2.2 Hz, 1H), 7.45 (d, J = 7.6 Hz, 1H), 7.38 (t, J = 7.8 Hz, 1H), 4.49 (s, 2H). ^{13}C: NMR: (126 MHz, DMSO) δ 166.33, 152.49, 146.78, 141.56, 139.61, 134.62, 129.28, 125.61, 121.69, 121.20, 118.22, 118.07. HRMS: calcd for $C_{14}H_{14}N_5O_4$ 316.1046, found 316.1054.

Synthesis of L

Intermediate **2**, 1-(3-(hydrazinecarbonyl)phenyl)-3-(4-nitrophenyl)urea (200 mg, 0.63 mmol), was taken in a 100 ml RB flask and suspended in 20 ml dry EtOH. Then 2-pyridinecarboxaldehyde (250 μl, 0.63 mmol) was added to the mixture and the reaction mixture was refluxed for another 6 h. A white precipitate appeared slowly. It was filtered with filter paper and the residue was washed with diethyl ether. A white solid was obtained as a pure product (600 mg, yield: 89%). ^{1}H NMR: (500 MHz, DMSO) δ 12.08 (s, 1H), 9.50 (s, 1H), 9.17 (s, 1H), 8.63 (d, J = 4.9 Hz, 1H), 8.50 (s, 1H), 8.21 (d, J = 8.9 Hz, 2H), 8.05 (s, 1H), 8.01 (d, J = 8.1 Hz, 1H), 7.90 (t, J = 7.8 Hz, 1H), 7.72 (t, J = 9.0 Hz, 3H), 7.59 (d, J = 7.8 Hz, 1H), 7.49 (t, J = 7.8 Hz, 1H), 7.44 (t, J = 6.2 Hz, 1H). ^{13}C NMR: (101 MHz, DMSO) δ 163.82, 153.73, 152.50, 149.99, 148.55, 146.71, 141.62, 139.88, 137.39, 134.49, 129.54, 125.62, 124.90, 122.53, 121.98, 120.41, 118.63, 118.12. HRMS: calcd for $C_{20}H_{17}N_6O_4$ 405.1311, found 405.1317.

Synthesis of EuC $[Eu(L)_2(OTf)_2(H_2O)](OTf)$

Ligand **L**, (*E*)-1-(4-nitrophenyl)-3-(3-(2-(pyridin-2-ylmethylene) hydrazine-1-carbonyl)phenyl)urea (300 mg, 0.74 mmol), was taken in a 100 ml RB flask and suspended in 20 ml dry methanol. Then europium(III) trifluoromethanesulfonate, $Eu(OTf)_3$ (221.63 mg, 0.37 mmol), was added to the mixture and the reaction mixture was refluxed for another 12 h. The suspension became a clear solution. The solvent was removed and a white solid was obtained. The precipitate was filtered with filter paper and the residue was washed with diethyl ether. A white solid was obtained as a pure product (511 mg, yield: 92%). ^{1}H NMR: (500 MHz, DMSO) δ 12.07 (s, 1H), 9.51 (s, 1H), 9.18 (s, 1H), 8.64 (s, 1H), 8.49 (s, 1H), 8.22 (d, J = 9.3 Hz, 3H), 8.05 (s, 1H), 8.00 (d, J = 8.0 Hz, 1H), 7.91 (t, J = 7.4 Hz, 1H), 7.76–7.69 (m, 4H), 7.59 (d, J = 7.8 Hz, 1H), 7.47 (dt, J = 23.0, 7.0 Hz, 3H). ^{13}C NMR (126 MHz, DMSO) δ 152.51, 150.04, 146.72, 141.62, 137.41, 129.55, 125.64, 124.89, 122.43, 121.98, 120.37, 119.87, 118.62, 118.12. HRMS: calcd for $C_{40}H_{32}N_{12}O_8^{2+}$ 480.5834, found 480.0728.

Fluorescence quantum yield (Φ) measurement

The fluorescence quantum yield (Φ) was calculated using a relative method using quinine bisulfate in 1 N H_2SO_4 (η = 1.338, Φ_{rel} = 54.6%) as a reference.[34,39,40] In this regard, we utilized a general equation:

$$\frac{\Phi_s}{\Phi_r} = \frac{A_r \eta_s^2 I_s}{A_s \eta_r^2 I_r} \quad (4)$$

where 'r' represents the reference and 's' the sample. '*A*' implies the absorbance at the excitation wavelength, whereas '*I*' is the integrated luminescence intensity, and 'η' represents the refractive index of the solvent (1.333 for solutions in water).

X-ray crystallography

Single-crystal X-ray diffraction was performed with a Bruker D8 Venture diffractometer, equipped with a MoKα radiation source, and a PHOTON III detector. The structures were solved using ShelXT[41] and refined with ShelxL[42] programs using Olex2[43] as a graphical user interface. Where disorder is present, necessary restraints for the same distance (SADI), similar Uij (SIMU), and a rigid body model (RIGU) were applied, if necessary.

The crystallographic data and refinement parameters are summarized in Table 1. The CIF file for **EuC** has been deposited with the Cambridge Crystallographic Data Centre (CCDC).

Computational details

All geometries reported in this study were fully optimized without symmetry constraints using the TURBOMOLE 7.7 program.[44] The BP86 functional, which combines the Becke exchange functional[45] and the Perdew correlation functional,[46] was employed for the calculations. The def2-TZVP basis set, as described by Weigend and Ahlrichs,[47] was used in conjunction with effective core potentials (ECPs) for the Eu element, following the work of Andrae *et al.*[48] These ECPs model the inner shell electrons and account for scalar relativistic effects. Long-

range dispersion interactions were accounted for using the D4 dispersion correction, developed by Grimme and co-workers.[49]

The COSMO solvation model, introduced by Klamt and Schüürmann[50] and further developed by Klamt,[51] was used to incorporate solvation effects. In particular, the COSMO model simulates the dielectric screening provided by the solvent, enhancing the realism of the calculations.

Conflicts of interest

There are no conflicts of interest to mention.

Data availability

The data supporting this article have been included as part of the supplementary information (SI). Supplementary information is available. See DOI: https://doi.org/10.1039/d5dt01849h.

CCDC 2414539 (**EuC**) contains the supplementary crystallographic data for this paper.[52]

Acknowledgements

The administration of Prabhat Kumar College in Contai is acknowledged by the corresponding author (TM) for their continuous support. TM expresses gratitude to the UGC DAE for the financial support *via* the project: Collaborative Research Scheme (CRS) (Ref: CRS/2022-23/02/839). Additionally, TM is grateful to DST FIST for their financial support of the College. The author would like to extend sincere thanks to Prof. Sujoy Baitalik, Department of Chemistry, Jadavpur University, for providing valuable scientific insights and guidance.

References

1 M. J. Langton, C. J. Serpell and P. D. Beer, *Angew. Chem., Int. Ed.*, 2016, **55**, 1974–1987.
2 N. Busschaert, C. Caltagirone, W. Van Rossom and P. A. Gale, *Chem. Rev.*, 2015, **115**, 8038–8155.
3 S. J. Butler and K. A. Jolliffe, *ChemPlusChem*, 2021, **86**, 59–70.
4 S. H. Hewitt, G. Macey, R. Mailhot, M. R. J. Elsegood, F. Duarte, A. M. Kenwright and S. J. Butler, *Chem. Sci.*, 2020, **11**, 3619–3628.
5 G. G. Yegutkin, *Biochim. Biophys. Acta, Mol. Cell Res.*, 2008, **1783**, 673–694.
6 P. Kumar, S. Pachisia and R. Gupta, *Inorg. Chem. Front.*, 2021, **8**, 3587–3607.
7 S. Sivagnanam, P. Mahato and P. Das, *Org. Biomol. Chem.*, 2023, **21**, 3942–3983.
8 S. H. Hewitt and S. J. Butler, *Chem. Commun.*, 2018, **54**, 6635–6647.
9 X. Zhang, J. Liu, J. Wang, L. Han, S. Ma, M. Zhao and G. Xi, *J. Photochem. Photobiol., A*, 2021, **223**, 112279.
10 Y. Kurishita, T. Kohira, A. Ojida and I. Hamachi, *J. Am. Chem. Soc.*, 2012, **134**, 18779–18789.
11 L. Reinke, M. Koch, C. Müller-Renno and S. Kubik, *Org. Biomol. Chem.*, 2021, **19**, 3893–3900.
12 A. Kumar, R. Pandey, A. Kumar, R. K. Gupta, M. Dubey, A. Mohammed, A. Mobi and D. S. Pandey, *Dalton Trans.*, 2015, **44**, 17152–17165.
13 M. Pushina, S. Farshbaf, S. Mochida, M. Kanakubo, R. Nishiyabu, Y. Kubo and P. A. Jr., *Chem. – Eur. J.*, 2021, **27**, 11344–11351.
14 T. Sakamoto, A. Ojida and I. Hamachi, *Chem. Commun.*, 2009, **2**, 141–152.
15 K. A. Jolliffe, *Acc. Chem. Res.*, 2017, **50**, 2254–2263.
16 S. J. Butler, *Chem. – Eur. J.*, 2014, **20**, 15768–15774.
17 S. L. Tobey and E. V. Anslyn, *J. Am. Chem. Soc.*, 2003, **125**, 14807–14815.
18 J. Sahoo, S. Jaiswar, H. S. Jena and P. S. Subramanian, *ChemistrySelect*, 2020, **5**, 12878–12884.
19 E. A. Weitz, J. Y. Chang, A. H. Rosenfield, E. A. Morrow and V. C. Pierre, *Chem. Sci.*, 2013, **4**, 4052–4060.
20 J. Sahoo, C. Krishnaraj, J. Sun, B. B. Panda, P. S. Subramanian and H. S. Jena, *Coord. Chem. Rev.*, 2022, **466**, 214583.
21 R. Mailhot, T. Traviss-Pollard, R. Pal and S. J. Butler, *Chem. – Eur. J.*, 2018, **24**, 10745–10755.
22 T. L. M. Martinon and V. C. Pierre, *Chem. – Asian J.*, 2022, **17**, e202200495.
23 S. E. Bodman, C. Breen, F. Plasser and S. J. Butler, *Org. Chem. Front.*, 2022, **9**, 5494–5504.
24 S. E. Bodman, C. Breen, S. Kirkland, S. Wheeler, E. Robertson, F. Plasser and S. J. Butler, *Chem. Sci.*, 2022, **13**, 3386–3394.
25 H. V. Barale and N. Dey, *RSC Adv.*, 2024, **14**, 25108–25114.
26 Z. Liao, Y. Liu, S.-F. Han, D. Wang, J.-Q. Zheng, X.-J. Zheng and L.-P. Jin, *Sens. Actuators, B*, 2017, **244**, 914–921.
27 M. Aarjane, S. Slassi and A. Amine, *J. Mol. Struct.*, 2020, **1199**, 126990.
28 V. Amendola, L. Fabbrizz and L. Mosca, *Chem. Soc. Rev.*, 2010, **39**, 3889–3915.
29 X. Wu, Q. Niu and T. Li, *Sens. Actuators, B*, 2016, **222**, 714–720.
30 N. Ahmed, I. Geronimo, I.-C. Hwang, N. J. Singh and K. S. Kim, *Chem. – Eur. J.*, 2011, **17**, 8542–8548.
31 J. Sahoo, R. Arunachalam, P. S. Subramanian, E. Suresh, A. Valkonen, K. Rissanen and M. Albrecht, *Angew. Chem., Int. Ed.*, 2016, **55**, 9625–9629.
32 M. Llunell, C. Casanova, J. Cirera, P. Alemany and S. Alvarez, *SHAPE, version 2.1*, Universitat de Barcelona, Barcelona, Spain, 2013.
33 T. Ahmed, A. Chakraborty, A. Paul and S. Baitalik, *Dalton Trans.*, 2023, **52**, 14027–14038.
34 T. Ahmed, A. Chakraborty and S. Baitalik, *Inorg. Chem.*, 2024, **63**, 11279–11295.

35 D. B. A. Raj, B. Francis, M. L. P. Reddy, R. R. Butorac, V. M. Lynch and A. H. Cowley, *Inorg. Chem.*, 2010, **49**, 9055–9063.
36 D. K. Singha, S. Bhattacharya, P. Majee, S. K. Mondal, M. Kumar and P. Mahata, *J. Mater. Chem. A*, 2014, **2**, 20908–20915.
37 S. V. Eliseeva, D. N. Pleshkov, K. A. Lyssenko, L. S. Lepnev, J.-C. G. Bünzli and N. P. Kuzmina, *Inorg. Chem.*, 2011, **50**, 5137–5144.
38 J. Baldwin, K. L. Bonham, T. R. C. Thompson, G. K. Gransbury, G. F. S. Whitehead, I. J. Vitorica-Erwzabal, D. Lee, N. L. Chilton and D. P. Mills, *JACS Au*, 2025, **5**, 1196–1212.
39 R. Biswas, P. Das, M. Das, S. Laha, A. Bag, U. K. Das, B. C. Samanta and T. Maity, *J. Photochem. Photobiol., A*, 2024, **452**, 115594.
40 P. Das, M. Das, R. Biswas, S. Laha, B. C. Samanta and T. Maity, *New J. Chem.*, 2024, **48**, 5820–5833.
41 G. M. Sheldrick, *Acta Crystallogr., Sect. A:Found. Adv.*, 2015, **71**, 3–8.
42 G. M. Sheldrick, *Acta Crystallogr., Sect. C: Struct. Chem.*, 2015, **71**, 3–8.
43 O. V. Dolomanov, L. J. Bourhis, R. J. Gildea, J. A. K. Howard and H. Puschmann, *J. Appl. Crystallogr.*, 2009, **42**, 339–341.
44 S. G. Balasubramani, G. P. Chen, S. Coriani, M. Diedenhofen, M. S. Frank, Y. J. Franzke, F. Furche, R. Grotjahn, M. E. Harding, C. Hättig, A. Hellweg, B. Helmich-Paris, C. Holzer, U. Huniar, M. Kaupp, A. M. Khah, S. K. Khani, T. Müller, F. Mack, B. D. Nguyen, S. M. Parker, E. Perlt, D. Rappoport, K. Reiter, S. Roy, M. Rückert, G. Schmitz, M. Sierka, E. Tapavicza, D. P. Tew, C. van Wüllen, V. K. Voora, F. Weigend, A. Wodyński and J. M. Yu, *J. Chem. Phys.*, 2020, **152**, 184107.
45 A. D. Becke, *Phys. Rev. A*, 1988, **38**, 3098.
46 J. P. Perdew, *Phys. Rev. B: Condens. Matter Mater. Phys.*, 1986, **33**, 8822.
47 F. Weigend and R. Ahlrichs, *Phys. Chem. Chem. Phys.*, 2005, **7**, 3297–3305.
48 D. Andrae, U. Haeussermann, M. Dolg, H. Stoll and H. Preuss, *Theor. Chem. Acc.*, 1990, **77**, 123–141.
49 E. Caldeweyher, S. Ehlert, A. Hansen, H. Neugebauer, S. Spicher, C. Bannwarth and S. Grimme, *J. Chem. Phys.*, 2019, **150**, 154122.
50 A. Klamt and G. Schüürmann, *J. Chem. Soc., Perkin Trans. 2*, 1993, 799–805.
51 A. Klamt, *J. Phys. Chem.*, 1995, **99**, 2224–2235.
52 CCDC 2414539: Experimental Crystal Structure Determination, 2025, DOI: 10.5517/ccdc.csd.cc2m1jcl.